

# FVNet: 3D Front-View Proposal Generation for Real-Time Object Detection from Point Clouds

Jie Zhou<sup>1</sup>, Xuequan Lu<sup>2</sup>, Xin Tan<sup>1</sup>, Zhiwen Shao<sup>1</sup>, Shouhong Ding<sup>3</sup>, Lizhuang Ma<sup>1</sup>

<sup>1</sup> Shanghai Jiao Tong University <sup>2</sup> Deakin University <sup>3</sup> Youtu Lab, Tencent

lordliang@sjtu.edu.cn, xuequan.lu@deakin.edu.au,  
{shaozhiwen, tanxin2017}@sjtu.edu.cn,  
ericshding@tencent.com, ma-lz@cs.sjtu.edu.cn

## Abstract

*3D object detection from raw and sparse point clouds has been far less treated to date, compared with its 2D counterpart. In this paper, we propose a novel framework called FVNet for 3D front-view proposal generation and object detection from point clouds. It consists of two stages: generation of front-view proposals and estimation of 3D bounding box parameters. Instead of generating proposals from camera images or bird’s-eye-view maps, we first project point clouds onto a cylindrical surface to generate front-view feature maps which retains rich information. We then introduce a proposal generation network to predict 3D region proposals from the generated maps and further extrude objects of interest from the whole point cloud. Finally, we present another network to extract the point-wise features from the extruded object points and regress the final 3D bounding box parameters in the canonical coordinates. Our framework achieves real-time performance with 12ms per point cloud sample. Extensive experiments on the 3D detection benchmark KITTI show that the proposed architecture outperforms state-of-the-art techniques which take either camera images or point clouds as input, in terms of accuracy and inference time.*

## 1. Introduction

3D object detection [3, 4, 10, 32, 24, 13] has become increasingly important in many fields, such as autonomous driving [1], mobile robots [27] and virtual/augmented reality [17]. While there have been remarkable progresses in the field of image-based 2D object detection, 3D object detection is far less explored than its 2D counterpart. The purpose of 3D object detection is to understand the geometry of physical objects in 3D space and predict future motion of objects. In this paper, we focus on 3D object detection from LiDAR, in which 3D bounding boxes of objects are pre-

dicted from raw point clouds. Compared with camera images, LiDAR point clouds are sparse and irregular (highly variable point density) because of the nonuniform sampling of the space, the radar coverage, the occlusion and relative attitude. How to encode point clouds for 3D object detection remains an interesting and open problem.

Deep neural networks usually take vectorized data as input, and the way of vectorizing point clouds is vital to the resulting performance. Some methods [28, 5, 32] voxelize point clouds into volumetric grids and then design voxel-wise feature extractors to handle them. However, since the captured point clouds in outdoor scenes are sparse in essence, the voxel grids are very sparse and therefore a large proportion of computation/memory is redundant and unnecessary. To obtain a more compact representation, some methods transform point clouds into 2D maps by projecting point clouds onto the ground plane (Bird’s Eye View) [2, 31, 26] or depth maps (Front View) [12, 16], and then apply 2D convolutional neural networks on the transformed maps to execute the detection task. The bird’s-eye-view representation can preserve the metric space and ease the problem of overlap, as objects usually do not overlap with each other. However, the bird’s-eye-view based methods often ignore the position and size along the  $Z$  axis. The assumption that objects of interest are constrained to the same ground plane is often unfeasible in practice. Besides, these methods are unfriendly to small objects such as pedestrians and cyclists, for example, BirdNet [2] and Complex-YOLO [26]. In comparison to the bird’s-eye-view representation, the front-view representation retains more information, which is similar to camera images. Inevitably, front-view representation has the same problem as camera images: the sizes of objects are closely related to the distances to scanners, and objects may overlap with each other. It is even more difficult to detect objects on the front-view maps than camera images, due to the loss of texture and color information. Consequently, previous front-view based

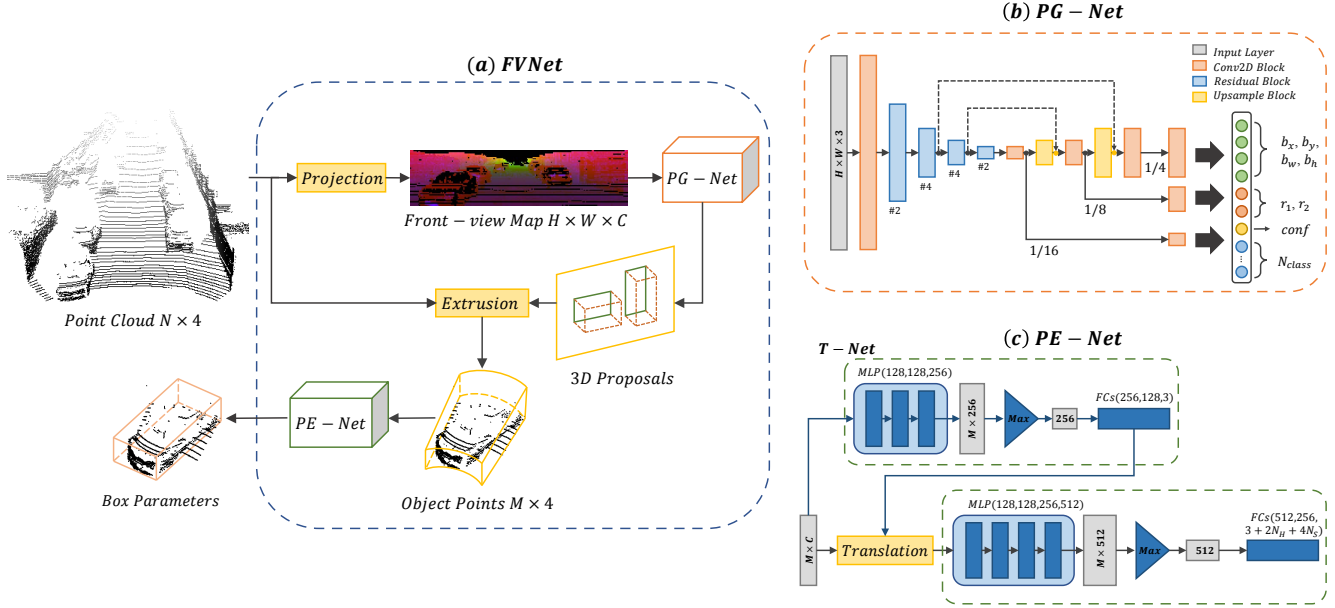


Figure 1. The overview of our (a) FVNet. It consists of two sub-networks: (b) Proposal Generation Network (PG-Net) for generation of 3D region proposals and (c) Parameter Estimation Network (PE-Net) for estimation of 3D bounding box parameters.

methods [18, 25] still utilize camera images to generate 2D proposals. However, these detectors based on camera images often miss objects due to dark lighting or dazzle light, and require high-quality synchronization between 2D camera sensors and 3D LiDAR sensors.

Motivated by the above problems, we propose a novel framework called FVNet for 3D object detection from raw point clouds (see Figure 1). It consists of two sub-networks: proposal generation network to generate 3D proposals and parameter estimation network to estimate bounding box parameters. For the detection of small objects, our detector is multi-scale so that it copes with the problem of large variance in object size. For the problem of overlap, our detector predicts accurate truncated radial distances to cut the view frustum for each single object. With predicting the truncated distances, we do not need an extra instance segmentation network to determine which points belong to the object of interest, avoiding suffering from computational complexity. To mitigate the problem of loss of texture and color information, we directly operate on the extruded object points to extract the point-wise features for estimating the final bounding box parameters. *Our method depends on point clouds only, without the need of camera images.* The main contributions of this work are summarized as follows.

- We propose a novel, multi-scale 3D object detector for predicting 3D bounding boxes of objects from raw point clouds.
- We introduce a proposal generation network to generate 3D proposals from front-view maps, without the

need of camera images. We extend 2D bounding boxes to 3D bounding boxes by truncating the frustum with truncated radial distances.

- We conduct extensive experiments, and show that our method outperforms state-of-the-art techniques which take either point clouds or camera images as input, in terms of accuracy and inference time. Our framework achieves real-time performance with 12ms per sample.

## 2. Related Work

We review previous works which are most relevant to this work. We first review the CNN-based object detection. We then investigate 3D object detection from point clouds, where the methods are categorized according to the encoding means for point clouds.

### 2.1. CNN-Based Object Detection

Real time and accuracy are key elements for autonomous driving which necessitates high prediction accuracy and efficiency of models. 2D detectors can be generally divided into two categories: single-stage and two-stage detectors. The two-stage detectors first inference proposals and then refine them, while single-stage detectors predict the final detection results directly. R-CNN [8] first generated category-independent region proposals and then extracted a fixed-length feature vector from each region with convolutional neural networks. Faster-RCNN [23] further improved the region proposal network and shared the feature representation with the detection network, leading to

further gain in both accuracy and speed. Despite that, it is still challenging by applying the typical two-stage pipelines to real-time applications. YOLO [20, 21, 22] and SSD [15] are two outstanding works with real-time speed. YOLO divided the image into sparse grids and made multi-class and multi-scale predictions per grid cell. SSD additionally used pre-defined anchors to handle large variance in object size and shape. Our method belongs to the single-stage detectors.

## 2.2. 3D Object Detection from Point Clouds

**Projection-Based Methods.** MV3D [4] hierarchically fused the CNN features extracted from the front view, bird’s eye view and camera view to jointly predict object class and regress the oriented 3D bounding boxes. PIXOR [30] took bird’s-eye-view representation as input alone and designed a proposal-free, single-stage detector to output pixel-wise predictions. It, however, assumes that all objects lie on the same ground and cannot handle indoor scenes where multiple objects often stack together in vertical space. Bird-Net [2] and RT3D [31] generated region proposals from bird’s-eye-view but achieve weak results. VeloFCN [12] is the first work to project point clouds onto a cylindrical surface. LMNet [16] took the front-view representation as input alone but got unsatisfactory results even on car detection, because of the loss of details. To ease the influence of the lack of details, we directly extract point-wise features from raw point clouds in our stage-2 sub-network (Sec. 3.2), rather than extracting pixel-wise features from the front-view or bird’s-eye-view maps as before.

**Voxel-Based Methods.** Voxel-based methods utilize a voxel grid representation for point clouds and involve differing ways to extract features. Vote3D [28] adopted sliding windows on sparse volumes to extract hand-crafted geometric features for each volume. Vote3Deep [5] introduced 3D convolutional neural networks to extract features for each volume. VoxelNet [32] built three voxel feature encoding (VFE) layers to extract 3D features for the region proposal network. However, the main issues of voxel representation are computational efficiency and memory consumption.

**Point-Based Methods.** F-Pointnet [18] and F-ConvNet [29] directly operated on raw point clouds by popping up RGB-D scans, without any loss of data, leading to precise detection. Their generation of object proposals depended largely on camera images. To get more accurate locations of objects, F-Pointnet adopted instance segmentation to classify the points in the view frustum while F-ConvNet divided the view frustum into a sequence of frustums to extract frustum-level features. Our approach also directly operates on raw point clouds, and our proposals are generated from point clouds only, without the need of camera images. We adopt the truncated distances to cut the view frustum for more accurate locations, without the

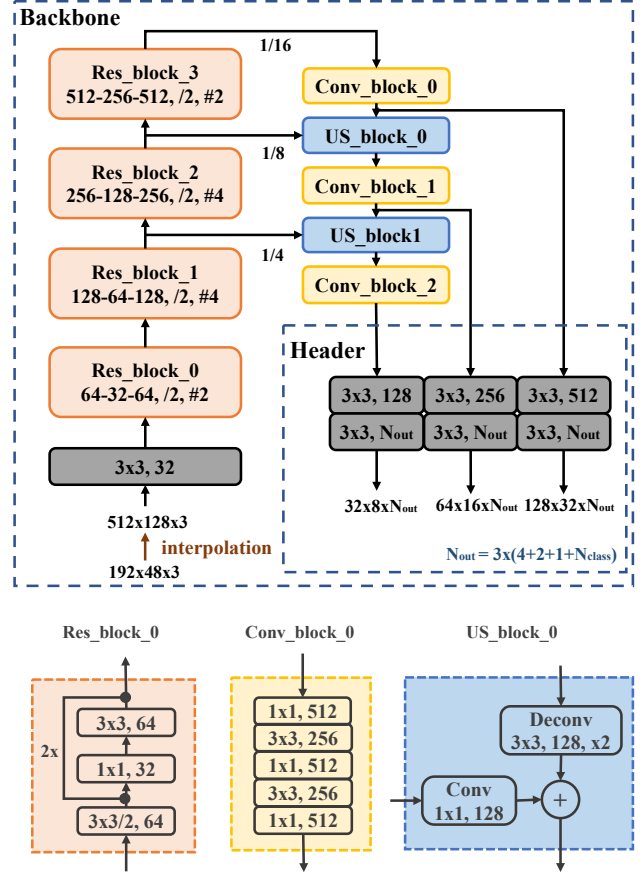


Figure 2. The architecture of our PG-Net. The bottom shows the details of the residual block, the convolutional block and the up-sampling block, respectively.

need of point cloud segmentation.

## 3. Proposed FVNet Framework

As shown in Figure 1, our 3D object detection framework consists of two sub-networks: Proposal Generation Network (PG-Net) and Parameter Estimation Network (PE-Net), respectively illustrated in (b) and (c). In this section, we introduce our two sub-networks in detail.

### 3.1. Proposal Generation Network

We design a multi-scale, fully-convolutional neural network for 3D proposal generation, and the network architecture is illustrated in Figure 2. The backbone network is to extract a general representation of the input in the form of convolutional feature maps. The header network is to make task-specific predictions.

**Data Preparation.** Different from the regular distribution of image pixels, the distribution of point clouds is usually sparse and irregular, which makes it challenging for di-

rect learning on point clouds. To circumvent this issue, we project the LiDAR point cloud onto a cylindrical surface for a dense, grid-based representation. This kind of representation combines the advantages of both image-based and 3D-based methods: (1) the easy extension of 2D convolutional neural networks from camera images to the front-view feature maps, (2) the ability of capturing dependencies across different views because of the depth information stored in the front-view maps. The projection functions are defined as follows:

$$\begin{aligned} \theta &= \arcsin \frac{z}{\sqrt{x^2 + y^2 + z^2}}, & r &= \lfloor \frac{\theta}{\Delta\theta} \rfloor, \\ \phi &= \arcsin \frac{y}{\sqrt{x^2 + y^2}}, & c &= \lfloor \frac{\phi}{\Delta\phi} \rfloor, \end{aligned} \quad (1)$$

where  $p = (x, y, z)^T$  denotes a point in 3D space and  $(r, c)$  denotes the 2D map position of its projection.  $\theta$  and  $\phi$  are the *azimuth* angle and the *zenith* angle, respectively.  $\Delta\theta$  and  $\Delta\phi$  are angle units.

By projecting a point cloud onto a cylindrical surface with Eq. 1, we can obtain a 3D tensor of size  $H \times W \times C$ .  $H$  and  $W$  are the height and width of the 2D map, respectively.  $C$  is the number of feature channels for each pixel. We fill the element at  $(r, c)$  with 3-channel features consisting of the height  $h = z$ , the radial distance  $r = \sqrt{x^2 + y^2}$  and the LiDAR intensity  $i$ . We visualize the three channels in RGB (Figure 1(a)). Compared with bird's-eye-view projection, projecting point clouds onto a cylindrical surface is based on angle instead of length, getting rid of the need of the scene range restriction.

The bounding boxes of small objects such as pedestrians and cyclists may be less than one pixel in size, due to the few details and small size of these objects in the front-view maps. Regarding this, we scale up the original front-view maps to a greater size by enhancing the details with the nearest neighbor interpolation. The nearest neighbor interpolation simply selects the value of the nearest pixel, yielding a piecewise-constant interpolant. Specifically, we enlarge the original front-view maps from  $48 \times 192$  to  $128 \times 512$  in our experiments.

**3D Proposals with Truncated Distances.** Thanks to the regularity of front-view feature maps, we can generate our 3D object region proposals on the top of mature 2D object detectors. 2D region proposals usually involve four parameters: the center coordinate  $(b_x, b_y)$  and the width and height of the bounding box,  $b_w$  and  $b_h$ . Different from 2D region proposals, 3D region proposals need more information to extrude the objects of interest from the frustum, due to the increase of dimension. F-Pointnet [18] adopted a 3D instance segmentation method (PointNet) to extract the object of interest from a point cloud in the view frustum by classifying the relevant and non-relevant points. Different

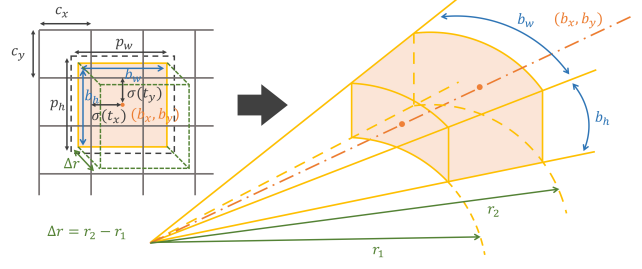


Figure 3. A 3D bounding box and its corresponding cylinder fragment. Left: the 3D bounding box with dimension prior ( $P_w, P_h$ ), location prediction ( $b_x, b_y$ ) and truncated distances prediction ( $r_1, r_2$ ). Right: the corresponding cylinder fragment in 3D space, which is generated by truncating the frustum with two radial distances  $r_1$  and  $r_2$ .

from their network, our PG-Net gets rid of instance segmentation. Our 3D proposals parse the 3D bounding boxes with six parameters  $(b_x, b_y, b_w, b_h, r_1, r_2)$ . As shown in Figure 3, we extend 2D bounding boxes to 3D bounding boxes by truncating the frustum with  $r_1$  and  $r_2$ .  $r_1$  and  $r_2$  denote the front and back truncated radial distances, respectively. Besides, we adopt a confidence score  $conf$  and  $N_{class}$  class scores for location and classification.

Following YOLOv3 [22], we use dimension clusters to generate pre-defined bounding box priors. We run the  $K$ -means clustering algorithm on the width and height of bounding boxes to get  $K$  reasonable bounding box priors. Our PG-Net predicts  $K/N_{scale}$  bounding boxes at each cell in each output layer, where  $N_{scale}$  is the number of output layers. We set  $N_{scale}$  to 3 in our experiments to favor different object sizes (large, medium and small). The network predicts  $4 + 2 + 1 + N_{class}$  values for each bounding box:  $t_x, t_y, t_w, t_h, t_{r_1}, t_{r_2}$ , the confidence score  $conf$  and  $N_{class}$  class scores. We predict the center coordinates relative to the location of the grid cell. Suppose the cell has an offset  $(c_x, c_y)$  from the top left corner of the feature map and the bounding box prior has width  $p_w$  and height  $p_h$ , the predictions can be computed as

$$\begin{aligned} b_x &= \sigma(t_x) + c_x, & b_y &= \sigma(t_y) + c_y, \\ b_w &= p_w e^{t_w}, & b_h &= p_h e^{t_h}, \\ r_1 &= t_{r_1} R, & r_2 &= t_{r_2} R, \end{aligned} \quad (2)$$

where  $R$  represents the maximum distance that LiDAR sensors can reach.  $\sigma(\cdot)$  refers to the sigmoid function for constraining the coordinate predictions to fall in  $[0, 1]$ .

We predict a confidence for each bounding box. When the bounding box prior has more overlaps with a ground-truth object than any other bounding box priors, its confidence is 1. When the bounding box prior is not the best but does overlap a ground-truth object by exceeding some threshold (e.g., 0.5), we ignore the prediction and its con-

fidence is 0. As a result, only one bounding box prior is assigned to a ground-truth object. It will lead to loss for confidence and no loss for coordinate or class predictions, if a bounding box prior is not assigned to a ground-truth object.

**Backbone Network.** With a similar concept to feature pyramid networks [14], our backbone network extracts features from three different scales for objects of different sizes. We show our backbone network architecture in Figure 2. It has a downsampling factor of 16 for the purpose of fewer layers in high resolution and more layers in low resolution. The backbone network composes of 4 residual blocks [9], 2 upsampling blocks and some convolutional layers. The first convolutional layer of each residual block has a stride of 2 in order to downsample the feature map. The numbers of skip connections are 2, 4, 4 and 2, respectively. Upsampling blocks are employed to get three final feature maps, with  $4\times$ ,  $8\times$  and  $16\times$  downsampling, respectively.

**Header Network.** The header network takes the three final feature maps from the backbone network as input, and outputs a 3D tensor for each branch. In our experiments, we predict 3 boxes at each scale and the tensor is  $M \times N \times [3 \times (4 + 2 + 1 + N_{class})]$  for 4 bounding box offsets, 2 truncated distances, 1 confidence prediction and  $N_{class}$  class predictions.

**Stage-1 Loss Function.** The multi-task loss  $L_{stage-1}$  for our PG-Net is an extension to the loss for 2D boxes. We apply the binary cross entropy loss on the location output  $p_{coord}$  (the center coordinates  $b_x$  and  $b_y$ ), the confidence output  $p_{conf}$  and the classification output  $p_{cls}$ . We apply a Huber loss on the regression output  $q$  for the width  $b_w$ , length  $b_h$  and truncated distances  $r_1$  and  $r_2$ .

$$L_{stage-1} = \lambda_{coord} B(p_{coord}, y_{coord}) + \lambda_{conf} B(p_{conf}, y_{conf}) + \lambda_{cls} B(p_{cls}, y_{cls}) + \lambda_{reg} H(q - y_{reg}), \quad (3)$$

where  $B(p, y)$  refers to the binary cross entropy loss function and  $H(x)$  indicates Huber loss function.  $\lambda_{coord}$ ,  $\lambda_{conf}$ ,  $\lambda_{cls}$  and  $\lambda_{reg}$  are weight coefficients, and  $y_{(\cdot)}$  denote the corresponding ground-truths. Considering that cars and persons may overlap in the front-view maps, we use multi-label binary cross entropy loss. These two loss functions can be computed as

$$B(p, y) = -\frac{1}{n} \sum_i (y[i] \log(p[i]) + (1 - y[i]) \log(1 - p[i])), \quad (4)$$

$$H(x) = \begin{cases} \frac{1}{2}x^2 & \text{if } |x| < \delta, \\ \delta|x| - \frac{1}{2}\delta^2 & \text{otherwise.} \end{cases} \quad (5)$$

### 3.2. Parameter Estimation Network

Given the learned 3D region proposals, we can extrude the object points of interest from the whole point cloud. We do data augmentation to the cropped point sets by random flipping, random rotation and bounding box perturbation. Our PE-Net extends the PointNet [19] structure to learn point-wise features and estimate the parameters of the amodal oriented 3D bounding box, including the box center coordinate  $(x, y, z)$ , the box size  $(h, w, l)$  and the heading angle  $\gamma$ .

**Network Architecture.** Inspired by PointNet [19], our PE-Net firstly employs the shared MLP on each point independently to extract local features, and then uses a max-pooling layer to descend the dimension of features. Finally, several fully connected convolutional layers are adopted to get the output. T-Net, involving only a MLP, is employed for the centroid alignment of the object points. The architecture of our PE-Net is shown in Figure 1(c).

**Stage-2 Loss Function.** To estimate the box center coordinates, we first normalize the extruded object points by subtracting the mean coordinate of points and then predict the residual box center coordinate, instead of directly predicting the original box center coordinate. For the box size and orientation estimation, we use a hybrid formulation of classification and regression. We equally split  $[0, 2\pi)$  into  $N_H$  angle bins, and thus PE-Net will output  $N_H$  scores for orientation classification and  $N_H$  residual angles for regression. Based on the above analysis, our stage-2 loss  $L_{stage-2}$  involves three components: center coordinate estimation, size estimation and orientation estimation, defined as

$$L_{stage-2} = L_{c1-reg} + L_{c2-reg} + L_{s-cls} + L_{s-reg} + L_{h-cls} + L_{h-reg} + L_{corner}, \quad (6)$$

where the corner loss  $L_{corner}$  proposed by [18] is a function joining the center, size and orientation.  $L_{corner}$  calculates the sum of the distances between the eight corners of a predicted box and a ground truth box, formulated as

$$L_{corner} = \sum_{i=1}^{N_S} \sum_{j=1}^{N_H} \delta_{ij} \min \left\{ \sum_{k=1}^8 \|P_k^{ij} - P_k^*\|, \sum_{k=1}^8 \|P_k^{ij} - P_k^{**}\| \right\}, \quad (7)$$

where  $\delta_{ij}$  is 1 for the ground-truth class and 0 elsewhere.

As illustrated in Figure 1, at test time, a point cloud of size  $N \times 4$  is firstly projected to a  $128 \times 512 \times 3$  front-view map which goes through PG-Net to generate 3D region proposals. Next the object points are extruded from the whole point cloud with 3D region proposals. In the second stage, the object points go through PE-Net and then output the final bounding box parameters.

Method	RGB	BEV	FV	Time	Car			Pedestrian			Cyclist		
					Easy	Mod.	Hard	Easy	Mod.	Hard	Easy	Mod.	Hard
MonoPSR [11]	✓			200	12.57	10.85	9.06	12.65	10.66	10.08	13.43	11.01	9.93
Stereo R-CNN [13]	✓			400	49.23	34.05	28.39	-	-	-	-	-	-
MV3D (LiDAR) [4]		✓	✓	240	<b>66.77</b>	52.73	51.31	-	-	-	-	-	-
BirdNet [2]		✓		110	14.75	13.44	12.04	14.31	11.80	10.55	18.35	12.43	11.88
RT3D [31]		✓		90	23.49	21.27	19.81	-	-	-	-	-	-
VeloFCN [12]			✓	1000	15.20	13.66	15.98	-	-	-	-	-	-
LMNet [16]			✓	20	-	15.24	-	-	11.46	-	-	3.23	-
<b>FVNet</b>			✓	<b>12</b>	65.43	<b>57.34</b>	<b>51.85</b>	<b>42.01</b>	<b>34.02</b>	<b>28.43</b>	<b>38.03</b>	<b>24.58</b>	<b>22.10</b>

Table 1. Performance comparison for **3D object detection** on KITTI *test* set with AP (%) and inference time (ms). “RGB”: camera images with RGB information. “BEV”: bird’s-eye-view maps. “FV”: front-view maps. The best results are highlighted in **bold**.

## 4. Experiments

In this section, we first describe the dataset and settings. We then compare our method with state-of-the-art 3D object detection methods on the KITTI [7] benchmark, in terms of both accuracy and inference time. Finally, we show some representative visual results and analyze our framework.

### 4.1. Dataset and Settings

**Dataset.** We use the challenging KITTI object detection benchmark [7] for training and evaluation. KITTI provides camera images and raw point clouds, including 7,481 sets for training and 7,518 sets for testing. *We only take the point clouds as input. The camera images are used for 3D bounding boxes visualization only.* Our method can handle the point clouds around 360°, but we only focus on the points within the camera’s FOV for simplicity. We empirically set the maximum radial distance  $R$  to 80 meters.

The “Pedestrian” category and the “Cyclist” category are quite similar on the front-view maps because both categories contain human body and have small pixel sizes. Given this, we only detect two classes, the “Car” category and the “Person” category (the sum of the “Pedestrian” category and the “Cyclist” category) in the proposal generation stage, and then distinguish the “Pedestrian” category from the “Cyclist” category in the parameter estimation stage. Thanks to the finer features extracted from the object points, pedestrians and cyclists can be easily identified. We start from scratch to train the model weights over the preprocessed feature maps.

**Implementation Details.** We train our PG-Net with a mini-batch size of 32 for  $10^5$  iterations and train PE-Net with a mini-batch size of 64 for  $2 \times 10^5$  iterations. It takes about 20 hours for training PG-Net and 13 hours for training PE-Net, with an NVIDIA 1080 Ti GPU and an i5-8600K 3.60GHz CPU. For data augmentation, we randomly crop and flip the front-view maps during PG-Net training, and apply random rotation in  $[-\pi/10, \pi/10]$  along the  $Z$  axis and random flip

along  $X$  axis during PE-Net training. We use non-maximal suppression (NMS) on front-view proposals with a threshold of 0.45 to remove overlapped proposals.

**Evaluation Metric.** Similar to previous works [12, 4, 30], we use the Average Precision (AP) [6] to evaluate the performance of our proposed framework. Following the KITTI setting, we do evaluation on three different regimes: *easy*, *moderate* and *hard*. The “Car” category is evaluated at 0.7 Intersection-Over-Union (IoU) while the “Pedestrian” and “Cyclist” categories are at 0.5 IoU. Similar to [12, 30], we ignore other categories in KITTI such as “Van” and “Person\_sitting”.

### 4.2. Comparison with State-of-the-Art Methods

We compare our approach with state-of-the-art methods [11, 13, 4, 2, 31, 12, 16], which are divided into two groups depending on the input (i.e., point clouds or camera images). One group consists of MonoPSR [11] (Mono-based) and Stereo R-CNN [13] (Stereo-based) which process camera images with RGB information. The other group includes MV3D (LiDAR) [4], BirdNet [2], RT3D [31], VeloFCN [12] and LMNet [16] which are based on point clouds only. All previous results are borrowed from the KITTI leadboard.

Table 1 reports the AP results and inference time of these methods. Compared with the camera-images-based methods, our method FVNet achieves significant better results despite using the raw point clouds only. Overall, our method performs best, except the car detection in *easy* setting by MV3D (LiDAR) which employs both front-view and bird’s-eye-view maps. Notice that most of the existing methods report no or very limited detection results on Pedestrian or Cyclist categories due to the challenge of these two categories. In contrast, our approach obtains competitive results, especially for the easy setting of Pedestrian (42.01% compared to 14.31% of BirdNet [2]). This demonstrates that our framework is effective for detecting small objects like pedestrians or cyclists.

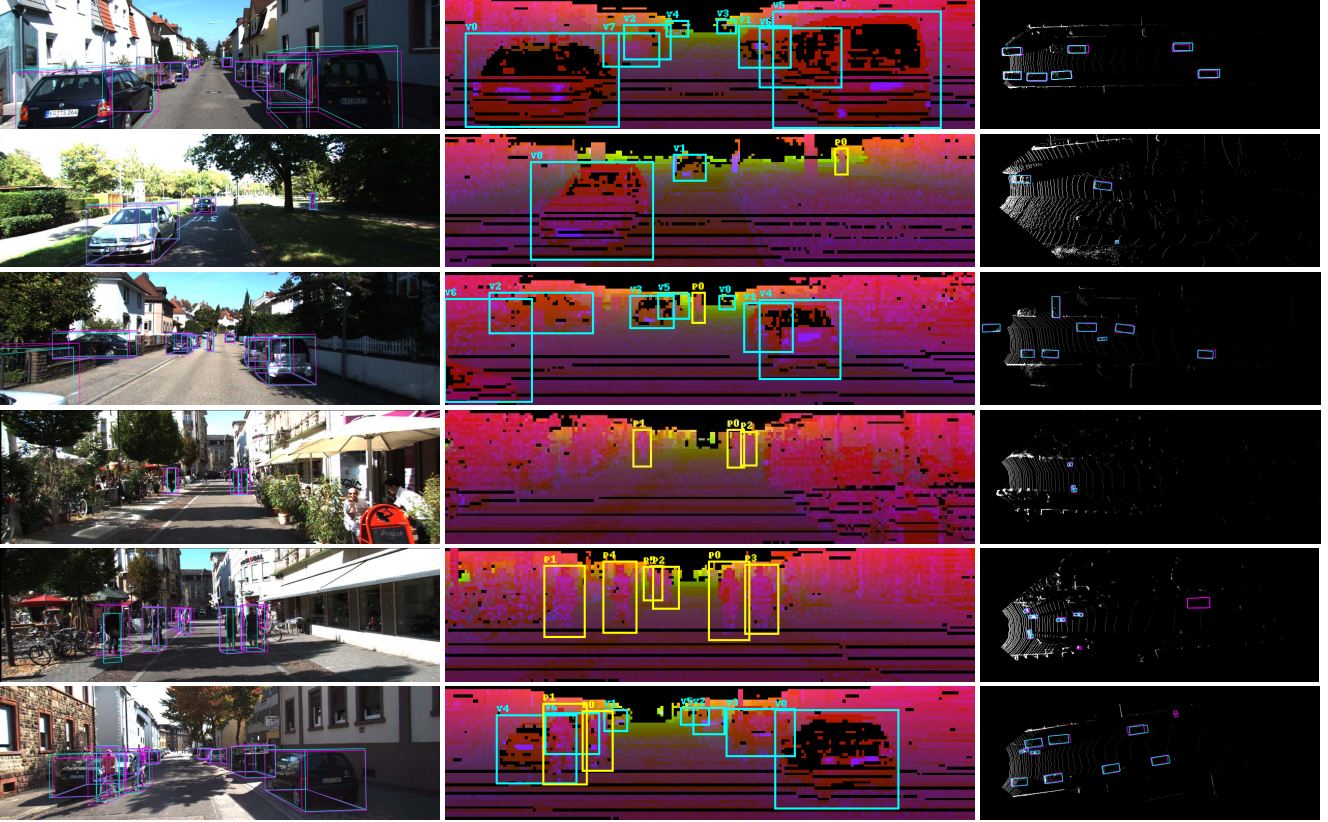


Figure 4. Visual results of 3D object detection by our FVNet. The left column shows the camera images with detected bounding box in blue and ground truth in red. The middle column shows the front-view maps with car predictions in blue and person predictions in yellow, and the right column shows the bird’s-eye-view maps with consistent colors with the left column (camera images). The notation attached to each bounding box denotes the detected object category, in which “V” and “P” indicate cars and people (including pedestrians and cyclists), respectively.

It can be observed that our method achieves the highest inference speed with only 12ms per sample. This is because that our framework generates high-quality 3D proposals from front-view maps directly, without the need of the instance segmentation network. Although LMNet [16] shows a comparable inference speed, its accuracy is remarkably lower than ours. MV3D (LiDAR) [4] performs generally the second best in accuracy but costs 20 times of inference time to ours.

### 4.3. Visual Results

We present six representative 3D object detection examples in Figure 4. It can be seen that our framework FVNet provides accurate 3D bounding boxes in all object categories. The top row shows that our method can easily deal with the dense cars. It can even detect small cars at a distance, such as the instances “V3” and “V4” in the corresponding front-view map. The second row demonstrates that our network can take small objects in the dark into account, for example, the instance “P0”, a pedestrian under

the shade of trees which is almost invisible in the bird’s-eye-view map. The third row indicates that even the object is hidden from view, our network can still predict its accurate size, such as the “V6” instance in the corresponding front-view map. The fourth and fifth rows show that our network has the ability to distinguish people from the crowd, including pedestrians and cyclists. From the last row we can see that when people overlap cars with a short distance, our network can separate them from each other clearly. In general, the proposed FVNet is applicable and robust in various cases, such as small objects, poor light conditions and slight occlusions.

### 4.4. Model Analysis

We analyze our framework from the aspects of 3D proposals, multi-scale detector and failure case.

**3D Proposals.** Figure 5 visualizes two examples of 3D proposals. Notice that these proposals are directly generated by our PG-Net rather than the final 3D bounding box predictions. It can be observed that the 3D proposals predicted

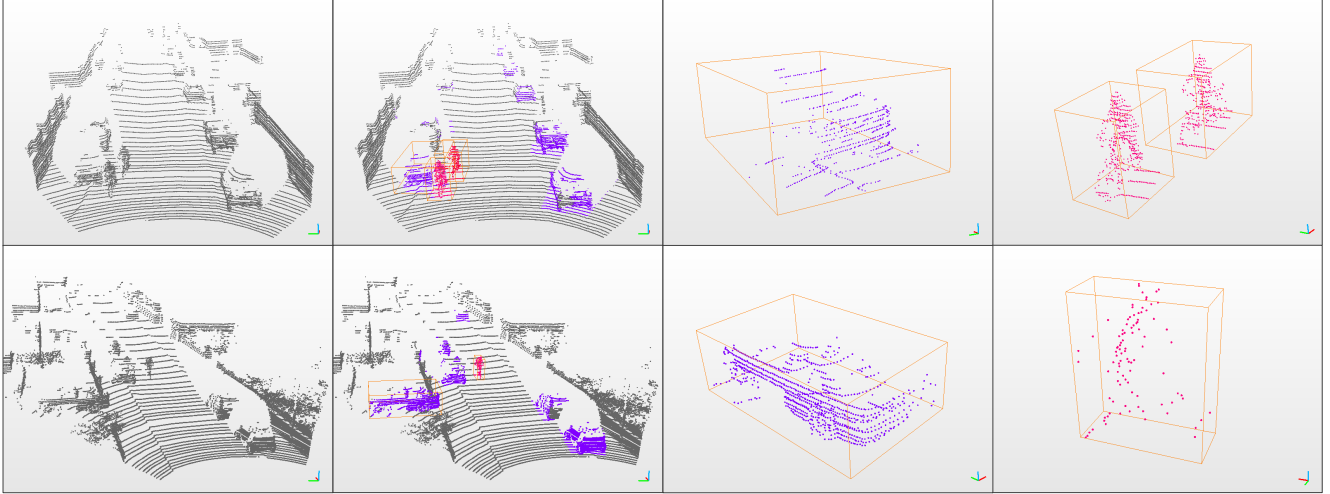


Figure 5. Visualization of 3D proposals generated by our PG-Net. The first column shows the raw point clouds with noise and outliers. The second column displays the 3D proposals in raw point clouds. The third column visualizes the predicted 3D proposals of cars, and the last column demonstrates the predicted 3D proposals of persons. The bounding boxes are to highlight the 3D proposals.

Setting	Scale	2D	AOS	BEV	3D
Easy	Single	75.42	74.22	63.79	50.97
	Multi	<b>86.14</b>	<b>85.94</b>	<b>78.04</b>	<b>65.43</b>
Mod.	Single	69.72	67.96	60.59	47.64
	Multi	<b>77.19</b>	<b>76.84</b>	<b>65.03</b>	<b>57.34</b>
Hard	Single	63.66	61.78	56.19	44.56
	Multi	<b>69.27</b>	<b>68.90</b>	<b>57.89</b>	<b>51.85</b>

Table 2. Evaluation on the Car category of KITTI *test* set using single-scale or multi-scale detectors. “2D”: AP of 2D object detection. “AOS”: average orientation similarity. “BEV”: AP of bird’s-eye-view object detection. “3D”: AP of 3D object detection. The results of “2D” and “BEV” are obtained by projecting our “3D” results to corresponding views directly. The best results of each setting are highlighted in **bold**.

from raw point clouds are convincing and reasonable. In the top row, persons with few pavements are included in the 3D proposals. In the last row, we can observe that the cars are correctly detected with clear shape of wheels. Since the results are comparable to those by instance segmentation, it is sufficient to accurately generate the final results with our 3D proposals.

**Multi-Scale Detector.** To evaluate the effectiveness of the proposed multi-scale detector, which aims to detect small objects at a distance, we also implement a single-scale variant of our framework. We compare our multi-scale detector with the single-scale detector on the Car category, shown in Table 2. It can be seen that the multi-scale detector achieves noticeably better accuracy, with margins of 14.5%, 9.7% and 7.3% in the settings of easy, moderate and hard for

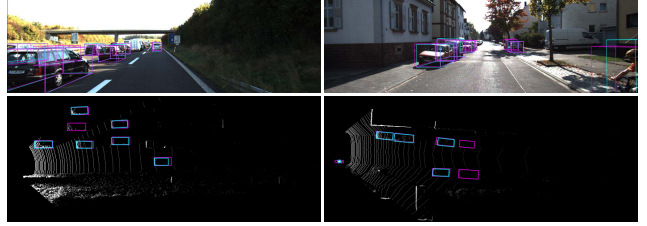


Figure 6. Failure cases: some objects are severely occluded. The first and second rows show results for camera images and the corresponding birds-eye-view maps, respectively. The detected bounding boxes and the corresponding ground-truth boxes are colored in blue and red, respectively.

3D object detection, respectively. This reveals that the proposed multi-scale detector is more effective than the single-scale version in detecting small objects.

**Failure Case.** Despite the proven accuracy and robustness, our method may fail in the case of severe occlusions. Some examples are showed in Figure 6, where some objects are occluded and the points are extremely sparse. As a result, the generated front-view maps are not reliable. This issue can be potentially alleviated by using the bird’s-eye-view maps, which we would like to investigate in the future.

## 5. Conclusion

In this paper, we have introduced a novel learning based approach for 3D object detection, which comprises of the proposal generation network and the parameter estimation network. Our method takes only point clouds as input, without the need of fusing other information like camera images. Extensive experiments show that our method outperforms state-of-the-art image-based techniques and

projection-based methods (point clouds as input), in terms of accuracy and inference time. Above all, our approach achieves real-time performance with 12ms per point cloud sample, and is significantly faster than other techniques.

## References

- [1] E. Ackerman. Lidar that will make self-driving cars affordable [news]. *IEEE Spectrum*, 53(10):14–14, 2016.
- [2] J. Beltrán, C. Guindel, F. M. Moreno, D. Cruzado, F. García, and A. De La Escalera. Birdnet: A 3d object detection framework from lidar information. In *IEEE International Conference on Intelligent Transportation Systems*, pages 3517–3523. IEEE, 2018.
- [3] X. Chen, K. Kundu, Z. Zhang, H. Ma, S. Fidler, and R. Urtasun. Monocular 3d object detection for autonomous driving. In *IEEE Conference on Computer Vision and Pattern Recognition*, pages 2147–2156. IEEE, 2016.
- [4] X. Chen, H. Ma, J. Wan, B. Li, and T. Xia. Multi-view 3d object detection network for autonomous driving. In *IEEE Conference on Computer Vision and Pattern Recognition*, pages 1907–1915. IEEE, 2017.
- [5] M. Engelcke, D. Rao, D. Z. Wang, C. H. Tong, and I. Posner. Vote3deep: Fast object detection in 3d point clouds using efficient convolutional neural networks. In *IEEE International Conference on Robotics and Automation*, pages 1355–1361. IEEE, 2017.
- [6] M. Everingham, L. Van Gool, C. K. Williams, J. Winn, and A. Zisserman. The pascal visual object classes (voc) challenge. *International Journal of Computer Vision*, 88(2):303–338, 2010.
- [7] A. Geiger, P. Lenz, C. Stiller, and R. Urtasun. Vision meets robotics: The kitti dataset. *International Journal of Robotics Research*, 32(11):1231–1237, 2013.
- [8] R. Girshick, J. Donahue, T. Darrell, and J. Malik. Rich feature hierarchies for accurate object detection and semantic segmentation. In *IEEE Conference on Computer Vision and Pattern Recognition*, pages 580–587. IEEE, 2014.
- [9] K. He, X. Zhang, S. Ren, and J. Sun. Identity mappings in deep residual networks. In *European Conference on Computer Vision*, pages 630–645. Springer, 2016.
- [10] J. Ku, M. Mozifian, J. Lee, A. Harakeh, and S. L. Waslander. Joint 3d proposal generation and object detection from view aggregation. In *IEEE/RSJ International Conference on Intelligent Robots and Systems*, pages 1–8. IEEE, 2018.
- [11] J. Ku, A. D. Pon, and S. L. Waslander. Monocular 3d object detection leveraging accurate proposals and shape reconstruction. In *IEEE Conference on Computer Vision and Pattern Recognition*. IEEE, 2019.
- [12] B. Li, T. Zhang, and T. Xia. Vehicle detection from 3d lidar using fully convolutional network. In *Robotics: Science and Systems*, 2016.
- [13] P. Li, X. Chen, and S. Shen. Stereo r-cnn based 3d object detection for autonomous driving. In *IEEE Conference on Computer Vision and Pattern Recognition*. IEEE, 2019.
- [14] T.-Y. Lin, P. Dollár, R. Girshick, K. He, B. Hariharan, and S. Belongie. Feature pyramid networks for object detection. In *IEEE Conference on Computer Vision and Pattern Recognition*, pages 2117–2125. IEEE, 2017.
- [15] W. Liu, D. Anguelov, D. Erhan, C. Szegedy, S. Reed, C.-Y. Fu, and A. C. Berg. Ssd: Single shot multibox detector. In *European Conference on Computer Vision*, pages 21–37. Springer, 2016.
- [16] K. Minemura, H. Liao, A. Monroy, and S. Kato. Lmnet: Real-time multiclass object detection on cpu using 3d lidar. In *Asia-Pacific Conference on Intelligent Robot Systems*, pages 28–34. IEEE, 2018.
- [17] Y. Park, V. Lepetit, and W. Woo. Multiple 3d object tracking for augmented reality. In *IEEE/ACM International Symposium on Mixed and Augmented Reality*, pages 117–120. IEEE, 2008.
- [18] C. R. Qi, W. Liu, C. Wu, H. Su, and L. J. Guibas. Frustum pointnets for 3d object detection from rgb-d data. In *IEEE Conference on Computer Vision and Pattern Recognition*, pages 918–927. IEEE, 2018.
- [19] C. R. Qi, H. Su, K. Mo, and L. J. Guibas. Pointnet: Deep learning on point sets for 3d classification and segmentation. In *IEEE Conference on Computer Vision and Pattern Recognition*, pages 652–660. IEEE, 2017.
- [20] J. Redmon, S. Divvala, R. Girshick, and A. Farhadi. You only look once: Unified, real-time object detection. In *IEEE Conference on Computer Vision and Pattern Recognition*, pages 779–788. IEEE, 2016.
- [21] J. Redmon and A. Farhadi. Yolo9000: better, faster, stronger. In *IEEE Conference on Computer Vision and Pattern Recognition*, pages 7263–7271. IEEE, 2017.
- [22] J. Redmon and A. Farhadi. Yolo3: An incremental improvement. *arXiv preprint arXiv:1804.02767*, 2018.
- [23] S. Ren, K. He, R. Girshick, and J. Sun. Faster r-cnn: Towards real-time object detection with region proposal networks. In *Advances in Neural Information Processing Systems*, pages 91–99, 2015.
- [24] S. Shi, X. Wang, and H. Li. Pointcnn: 3d object proposal generation and detection from point cloud. *arXiv preprint arXiv:1812.04244*, 2018.
- [25] K. Shin, Y. P. Kwon, and M. Tomizuka. Roarnet: A robust 3d object detection based on region approximation refinement. *arXiv preprint arXiv:1811.03818*, 2018.
- [26] M. Simon, S. Milz, K. Amende, and H.-M. Gross. Complex-yolo: An euler-region-proposal for real-time 3d object detection on point clouds. In *European Conference on Computer Vision*, pages 197–209. Springer, 2018.
- [27] C. Sprunk, G. D. Tipaldi, A. Cherubini, and W. Burgard. Lidar-based teach-and-repeat of mobile robot trajectories. In *IEEE/RSJ International Conference on Intelligent Robots and Systems*, pages 3144–3149. IEEE, 2013.
- [28] D. Z. Wang and I. Posner. Voting for voting in online point cloud object detection. In *Robotics: Science and Systems*, pages 10–15607, 2015.
- [29] Z. Wang and K. Jia. Frustum convnet: Sliding frustums to aggregate local point-wise features for amodal 3d object detection. *arXiv preprint arXiv:1903.01864*, 2019.
- [30] B. Yang, W. Luo, and R. Urtasun. Pixor: Real-time 3d object detection from point clouds. In *IEEE Conference*

- on *Computer Vision and Pattern Recognition*, pages 7652–7660. IEEE, 2018.
- [31] Y. Zeng, Y. Hu, S. Liu, J. Ye, Y. Han, X. Li, and N. Sun. Rt3d: Real-time 3-d vehicle detection in lidar point cloud for autonomous driving. *IEEE Robotics and Automation Letters*, 3(4):3434–3440, 2018.
- [32] Y. Zhou and O. Tuzel. Voxelnet: End-to-end learning for point cloud based 3d object detection. In *IEEE Conference on Computer Vision and Pattern Recognition*, pages 4490–4499, 2018.